Acoustic spin-controlled orbital rotations in double spiral acoustic beams

Check for updates
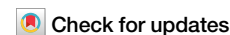
Di-Chao Chen[1,2,3], Xie Liu[1,3], Da-Jian Wu [1] ✉, Xing-Feng Zhu[1,2], Qi Wei[1], Ying Cheng [2] ✉ & Xiao-Jun Liu [2] ✉

Similar to optical spin-orbit interactions (SOIs), acoustic SOIs are anticipated to offer fresh perspectives and capabilities for acoustic manipulation beyond conventional scalar degrees of freedom. However, the acoustic extrinsic SOIs caused by particular properties of the medium were seldom explored. Here, the acoustic extrinsic SOI is observed in a double spiral acoustic beam (DSAB), as evidenced by the rotation of the spatial intensity pattern along the propagation axis. The interaction of the acoustic plane wave with the well-designed artificial flat structure generates two non-paraxial focused acoustic vortices (NFAVs) with different spin angular momentums. The coaxial coupling between them leads to acoustic spin-controlled orbital rotation (SOR). Theoretical formulations, supported by numerical simulations and experimental results, are provided to demonstrate the validity of acoustic SOR. Our work provides new perspectives and capabilities for understanding sound processing, and may open an avenue for the development of spin-orbit acoustics.

Spin-orbit interactions (SOIs) of light have greatly advanced our knowledge of the fundamentals of light[1–3] and facilitated various emerging applications, including high-resolution microscopy[4], beam shaping with planar structures[5], quantum information processing[6,7], and optical micro-manipulations[8]. The most fundamental and significant SOI of light is the interaction between orbital angular momentum (OAM)[9–11] and spin angular momentum (SAM)[12,13]. Two main types of optical SOI are intrinsic SOI and extrinsic SOI. The intrinsic SOI originates from the fundamental properties of Maxwell's equations while the extrinsic SOI is caused by specific features of medium[14]. In contrast to light waves described by vector fields, it was widely believed that, although acoustic waves can carry OAMs[15–20], the curl-free nature of longitudinal waves prevents them from having SAM[21,22]. Recent studies have shown that the longitudinal vector field of an inhomogeneous acoustic wave can possess a locally rotational velocity field that is considered to be acoustic spin[23–27]. Similar to the optical spin, the acoustic spin is considered as a rotation of the wave polarization given by its local particle velocity[14,28]. An example of the inhomogeneous beam is the non-paraxial acoustic vortex whose velocity field exhibits a polarization circular in the transverse cross-section and hence produces the longitudinal SAMs[21]. Meanwhile, OAMs also can be produced in the real-space field by its azimuth-dependent mutual phase. Furthermore, it was discovered that the SAM and OAM of the non-paraxial acoustic vortex can be converted with the cone angle. This is an intrinsic SOI effect arising from the fundamental nature of the acoustic linear equations[14,29]. More recently, Alhaïtz et al. considered the extrinsic SOI effect, where the angular momentum form is transformed between spin and orbital through the

interaction between an acoustic evanescent wave and an isolated droplet[30]. However, the acoustic extrinsic SOIs in traveling waves were seldom reported, primarily because the extrinsic SOI effect is triggered by unique medium properties. Realizing acoustic extrinsic SOI is a challenging task for acoustic traveling waves that necessitates the exploration of anisotropic media possessing specific features.

In this work, the acoustic extrinsic SOI is observed in a double spiral acoustic beam (DSAB), as evidenced by the rotation of the spatial intensity pattern along the propagation axis. The three-dimensional representation of the DSAB with a rotating spatial intensity pattern is shown in Fig. 1. The interaction of the acoustic plane wave with a well-designed composite artificial structure plate (ASP) generates two NFAVs with different SAMs and opposite topological charges (TCs). Since SOI in the non-paraxial focused acoustic vortex (NFAV) is accompanied by a decomposition of the propagation constant, the coaxial coupling of two NFAV beams with different propagation constants can produce rotational beating effects, resulting in acoustic spin-controlled orbital rotations[31,32]. The theoretical predictions of the generations of the DSAB and acoustic spin-controlled orbital rotations have been well demonstrated by the numerical simulations. Finally, we fabricate the composite ASP sample to realize the DSAB experimentally and verify the acoustic SOR.

Results

Generation of the non-paraxial focused acoustic vortex

We designed an artificial flat structure (AFS) to produce an NFAV. Studies have reported the generation of vortex acoustic beams using artificial plate

[1]School of Physics and Technology, Nanjing Normal University, 210023 Nanjing, China. [2]Department of Physics, Nanjing University, 210093 Nanjing, China. [3]These authors contributed equally: Di-Chao Chen, Xie Liu. ✉e-mail: wudajian@njnu.edu.cn; chengying@nju.edu.cn; liuxiaojun@nju.edu.cn

structures. However, previous studies have not considered the variation of radial wave number k_r and axial wave number k_z during propagation and the effect of the variation of k_r and k_z on the generated vortex acoustic beams. Additionally, there is no report on the interpretation and analysis of the SAM and OAM of the vortex acoustic beam generated by the artificial plate structure, and these will be the focus of what we will discuss next. The helical phase dislocation of the focused wave front, which creates the OAM, is one typical feature of the NFAV. The wave vector forming a cone at the angle α is another characteristic[15–17,33,34]. The cone angle α determines the phase velocity decomposition that occurs in NFAV along with the interconversion between SAM and OAM.

The phase velocity decomposition indicates that different cone angles accumulate phase at different rates depending on the distance. Figure 2a shows the schematic diagram of an AFS for achieving an NFAV beam with TC of $l = 1$. 56 discrete circular holes are engraved on the AFS and arranged on 8 lines with an adjacent azimuth of $\pi/4$. Each line includes 7 circular holes. It should be noted that the suggested composite ASPs with holes of various geometries are all capable of producing NFAVs and the intensity of the resulting NFAV is enhanced with increasing hole size. In this case, the

Fig. 1 | The double spiral acoustic beam generated by a composite artificial structural plate (ASP). Schematic diagram of the acoustic rotating double spiral beam space pattern in spin-controlled orbital rotation (SOR) realized by an artificial structure. The red element represents a double spiral high-intensity focus.

geometry of the hole is set as a rounded shape to make sample production easier. The radius of the circle hole is a and the polar coordinate of the nth circle hole is defined as (r_n, φ_n),

$$\begin{cases} r_n^2 = \left[\sqrt{r_0^2 + f_z^2} + \frac{\varphi_n \lambda}{2\pi} + m\lambda \right]^2 - f_z^2 \\ \varphi_n = \pi[\mathbf{mod}(n-1,\ 8) - 4]/4 \end{cases} \quad (1)$$

where f_z is the focal length, λ is the wavelength, $m = \mathbf{floor}\left[(n-1)/8\right] - 3$, and the constant r_0 is defined as the initial radius. The operators mod and floor are used to perform modulo and downward rounding operations on complex functions, respectively. As shown in the partial enlarged drawing of Fig. 2a, the first 8 circular holes locate on a spiral. Figure 2b shows the three-dimensional diagram of the first 8 circular holes with $m = -3$, where α is the angle between the line connecting the transmission point and the observation point and the z-axis. The distance from the nth hole to the focus is $L_n = \sqrt{f_z^2 + r_n^2}$, According to Eq. (1), the phase difference between two adjacent circle holes to the focus is $\Delta L_n 2\pi/\lambda = \pi/4$. After accumulating, a linear phase shift of 2π is realized by the first 8 circular holes, which meets requirements of an AV with TC l of 1. The acoustic field at the observation point (ρ, θ, z) in column coordinates can be calculated by[35]

$$p(\rho, \theta, z, t) = \exp(-i\omega t) \sum_{n=1}^{8} \left[\frac{A_0}{R_n} \exp(i\vec{\mathbf{k}}_{\mathbf{n}} \cdot \vec{\mathbf{R}}_{\mathbf{n}}) \right] \quad (2)$$

where A_0 is a real constant, ω is the angular frequency and t denotes time. $R_n (= \sqrt{(\rho\cos\theta - r_n\cos\varphi_n)^2 + (\rho\sin\theta - r_n\sin\varphi_n)^2 + z^2})$ is the distance between the nth circle hole and the observation point (ρ, θ, z), ρ is the distance from the origin O to the projection of the observation point on the plane xoy. From the positive z-axis, θ is the angle turned from the x-axis in a counterclockwise direction to the projection, z is the height of the observation point. $\vec{\mathbf{k}}_{\mathbf{n}}$ is the wave vector of the wave generated by the nth circle hole, whose direction points from the hole to the observation point. $\vec{\mathbf{R}}_{\mathbf{n}}$ and $\vec{\mathbf{k}}_{\mathbf{n}}$ have the same vector direction. As shown in Fig. 2b, $\vec{\mathbf{k}}_{\mathbf{n}}\vec{\mathbf{R}}_{\mathbf{n}}$ can be decomposed into two parts of $k_{nr}r_n$ and $k_{nz}z$, where k_{nr} and k_{nz} are the radial and axial wavenumbers of the nth hole, respectively. This allows

Fig. 2 | Schematic illustration of the designed artificial flat structure (AFS). a Schematics of the artificial structures for achieving a non-paraxial focused acoustic vortex (NFAV) with $l = 1$ for topological charge (TC). Numbers 1–8 represent the nth circular holes separately. **b** Diagram of the first holes of the eight azimuth angles and the coordinates used in analytical derivation. L is the distance from the 6$^{\text{th}}$ hole to the focus. k_r and k_z are the radial and axial wavenumbers of the 6th hole. **c** Schematic diagram of the cross-section of the artificial structure.
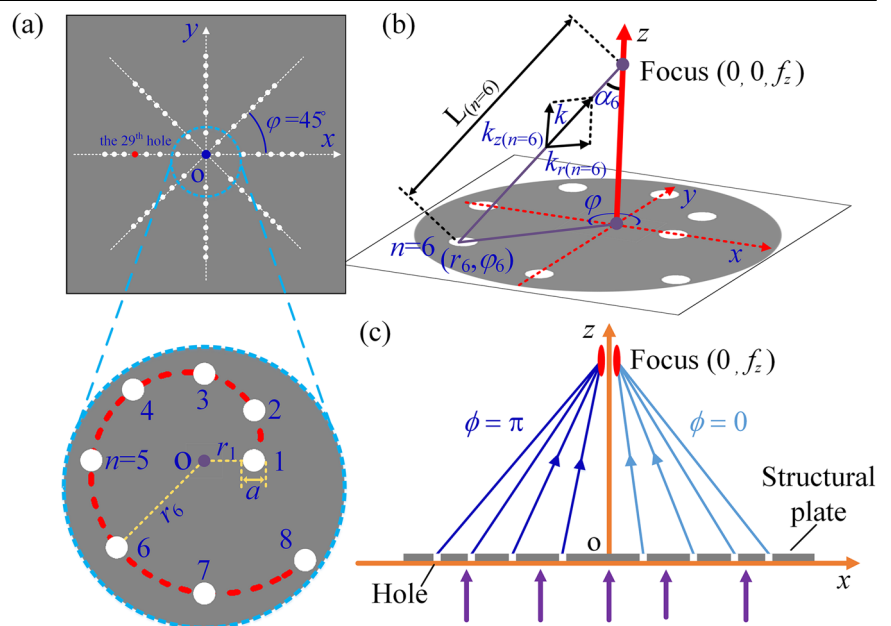
Eq. (2) to be rewritten as[36,37]

$$p(\rho,\theta,z,t) = \exp(-i\omega t)\sum_{n=1}^{8}\frac{A_0}{R_n}\exp(ik_{nz}z)\exp\left[i\vec{k}_{nr}\cdot(\rho\hat{e}_\rho - r_n\hat{e}_{r_n})\right] \qquad (3)$$

According to Eq. (1), r_n also can be rewritten as $r_n = r_0 + r_m + \Delta r_n, (m = -3)$, where

$$\begin{cases} r_m = \sqrt{\left[\sqrt{r_0^2+f_z^2}+m\lambda\right]^2-f_z^2}-r_0 \\ \Delta r_n = \sqrt{\left[\sqrt{r_0^2+f_z^2}+\varphi_n\lambda/2\pi+m\lambda\right]^2-f_z^2}-\sqrt{\left[\sqrt{r_0^2+f_z^2}+m\lambda\right]^2-f_z^2} \end{cases} \qquad (4)$$

Considering $\sqrt{r_0^2+z^2}+m\lambda \gg \frac{\varphi_n\lambda}{2\pi}$ for the observation points near the focal area, we can rewrite R_n as $R_n \approx \sqrt{r_n^2+z^2} = \sqrt{r_0^2+z^2}+m\lambda$. Thus, Eq. (3) can be further approximated as

$$p(\rho,\theta,z,t) \approx \frac{A_0}{\sqrt{r_0^2+z^2}+m\lambda}\exp(-i\omega t)\exp(ik_{nz}z)\exp[-ik_{nr}(r_0+r_m)] \qquad (5)$$
$$\times\sum_{n=1}^{8}\exp[i\rho k_{nr}\cos(\theta-\varphi_n)]\exp(-ik_{nr}\Delta r_n)$$

where $k_{nz} = k\cos(\alpha_n) \approx kz/\left(\sqrt{r_0^2+z^2}+m\lambda\right), (m = -3)$ and $k_{nr} = \sqrt{k^2-k_{nz}^2}$. The product of k_{nr} and Δr_n is approximately equal to φ_n. Thus, $\sum_{n=1}^{8}\exp[i\rho k_{nr}\cos(\theta-\varphi_n)]\exp(-ik_{nr}\Delta r_n)$ can be viewed as a discrete quantity of the Jacobi-Anger expansion, which can be approximated as equal to $\int_{-\pi}^{\pi}\exp[i\rho k_{nr}\cos(\theta-\varphi)]\exp(-i\varphi)d\varphi = \exp[i(\theta-\frac{\pi}{2})]2\pi J_1(k_{nr}\rho)$. Then, Eq. (5) can be simplified as

$$p(\rho,\theta,z,t) \approx A_n\exp(-i\omega t)\exp(ik_{nz}z)\exp(i\theta)J_1(k_{nr}\rho) \qquad (6)$$

where $A_n = \frac{A_0}{\sqrt{r_0^2+z^2}+m\lambda}2\pi\exp[-ik_{nr}(r_0+r_m)-i\frac{\pi}{2}], (m = -3)$, J_1 is a first order Bessel function. Thus, the first 8 circle holes could approximately produce a first order Bessel vortex beam with TC of 1. According to Eq. (1), the range difference to the focal point between every 8 circular holes is λ, i.e., the phase shift of 2π, as shown in Fig. 2c. As a result, the constructive interfering of seven Bessel vortex acoustic beams can be generated by the AFS with 56 circular holes.

$$P(\rho,\theta,z,t) \approx \exp(i\theta)\exp(-i\omega t)\sum_{m=-3}^{3}A_n^m\exp(ik_{nz}^m z)J_1(k_{nr}^m\rho) \qquad (7)$$

k_{nz}^m also can be written as $k_{nz} \approx k_z + \Delta k_z^m$, where $k_z = kz/\sqrt{r_0^2+z^2}$ and $\Delta k_z^m = kz/\sqrt{r_0^2+z^2} - kz/\left(\sqrt{r_0^2+z^2}+m\lambda\right)$. Provided $\sqrt{r_0^2+z^2} \gg m\lambda$, one can simplify k_{nz} by approximating $k_{nz} \approx k_z$, and hence $k_{nr}^m = k_r = \sqrt{k^2-k_z^2}$. Finally, Eq. (7) can be rewritten as

$$P(\rho,\theta,z,t) \approx A\exp(-i\omega t)\exp(i\theta)\exp(ik_z z)J_1(k_r\rho) \qquad (8)$$

where $A \approx \frac{A_0}{\sqrt{r_0^2+z^2}}2\pi\exp[-ik_r r_0 - i\frac{\pi}{2}]$. With the time-dependent pressure field we can obtain the vector velocity part of the acoustic Bessel field from the equation $v = -i(\delta w)^{-1}\nabla P$, which yields

$$v_x = -i\frac{Ak_r}{2\delta\omega}\left[J_0(k_r\rho)\exp(-i\theta)+J_2(k_r\rho)\exp(i\theta)\right]\exp(i\theta+ik_z z-i\omega t)$$
$$v_y = \frac{Ak_r}{2\delta\omega}\left[J_0(k_r\rho)\exp(-i\theta)+J_2(k_r\rho)\exp(i\theta)\right]\exp(i\theta+ik_z z-i\omega t) \qquad (9)$$

where δ is mass density, J_0 and J_2 are zero order Bessel function and second order Bessel function, respectively. From this, we find that the polarization of the velocity field in the center of the vortex beam is always purely circular, with the handedness determined by the sign of l. Substituting the velocity component (8) into the acoustic SAM density expression $S = \frac{\delta}{2\omega}\text{Im}(v^*\times v)$, the longitudinal component can be expressed as[15]

$$S_z = \frac{\beta|A|^2}{4\omega}\sin^2\alpha\left[J_0^2(k_r\rho)-J_2^2(k_r\rho)\right] \qquad (10)$$

where the compressibility $\beta = 1/B$ (B is the bulk modulus). From Eq. (10), it can be seen that the value of S_z is maximum when it is on the propagation axis and increases gradually with the increase of cone angle α, while S_z vanishes when $J_0^2(k_r\rho) = J_2^2(k_r\rho)$. Using the Bessel recursive formula $\frac{d}{d\rho}(J_1(k_r\rho)) = \frac{1}{2}\left[J_0(k_r\rho)-J_2(k_r\rho)\right]$, we find that S_z vanishes at the high acoustic intensity position of the Bessel vortex beams. The longitudinal spin density direction is represented by the unit vector $\hat{s} = S_z/|S_z| = \sigma s$. The spin handedness, or helicity, is $\sigma = \pm 1$ and $s = 1$ for the particles on the z-axis. We call $\sigma = -1$ left-handed polarization and $\sigma = 1$ right-handed polarization. The z-component of the OAM density can be calculated as $O_z = l\frac{W}{\omega} - \frac{S_z}{2}$, where W is the time-averaged energy density[21], which can be obtained from $W = \frac{1}{4}(\beta|P|^2 + \delta|v|^2)$. This means that NFAV beams can be considered as eigenmodes of the total angular momentum operator rather than of the OAM operator and the SAM operator, separately. This is analogous to the result of intrinsic SOIs in vector light or quantum fields, which can enable interconversion between SAM and OAM[25,26]. In the paraxial limit (i.e. $\alpha \leq 20°$), $\alpha \approx \sin\alpha \ll 1$, the radial distribution of the W and SAM vanishes in the center of focused vortices. When it comes to the non-paraxial regime, the focused vortices with $l = 1$ have nonzero W and SAM in the center. Therefore, it is necessary to generate NFAV to implement acoustic SOI. In addition, from Eq. (8), by convergent cone angle, we can decompose the wave number k into the axial wave number k_z along the propagation direction of the NFAV and the radial wave number k_r, and the process of wave number decomposition is called wave number decomposition. The wave number can also be expressed as the rate of change of phase with distance, and thus the decomposition can also be expressed as a decomposition of the phase velocity. The SOI in NFAV is accompanied by a decomposition of the propagation constant (phase velocity), and NFAVs with different cone angles have different propagation constants k_z.

Next, we verify the generation of the NFAV using the proposed AFS. Figure 3a shows the acoustic intensity profile in the x-z plane based on Eq. (2). The background medium is air with the mass density of 1.21 kg m^{-3} and the sound speed of 343 m s^{-1}. The working frequency is fixed at 15 kHz ($\lambda = \sim22.9$ mm). Here, $r_1 = 40$ mm, $f_z = 280$ mm (12.2λ), and thus the cone angle is $\alpha = \sim$ (satisfying the condition of non-paraxial). The theoretically obtained acoustic intensity distribution and phase distribution in the focal plane are shown in Fig. 3b. The phase distribution shows a typical screw dislocation with $l = 1$ for TC. The toroidal acoustic intensity distribution clearly shows the axial zero characteristic of a highly focused vortex beam. By measuring the time-dependent pressure field P, the vector velocity parts v_x and v_y in the x-y plane can be derived. We find that the polarized form at the center of the NFAV is approximately purely circular and the handedness is consistent with the sign of l, as shown in the enlarged drawing of Fig. 3b, which is consistent with theoretical predictions. The black arrow and the arrowed red circle denote the polarization of the velocity field and its time evolution. Then, the numerical simulations of our design are performed using the FEM (via the COMSOL Multiphysics software). Figure 3c shows the x-z plane normalized simulated acoustic distribution. Figure 3d represents the normalized acoustic intensity and phase distribution of the NFAV in the focal plane obtained from the simulation. Here, the radius of the circle hole a is fixed at 5 mm, the AFS is set to be acoustically rigid, and the other parameters are the same as those in the theoretical calculation. It can be seen that the simulations match well with the analytical results. Especially, the simulation polarization at the center of the focused region is approximately purely circular, which is in agreement with the theoretical results. The axial distributions [marked by dashed "I" in Fig. 3a, c] and radial distributions [marked by dashed "II" in Fig. 3a, c] of acoustic intensity are shown in
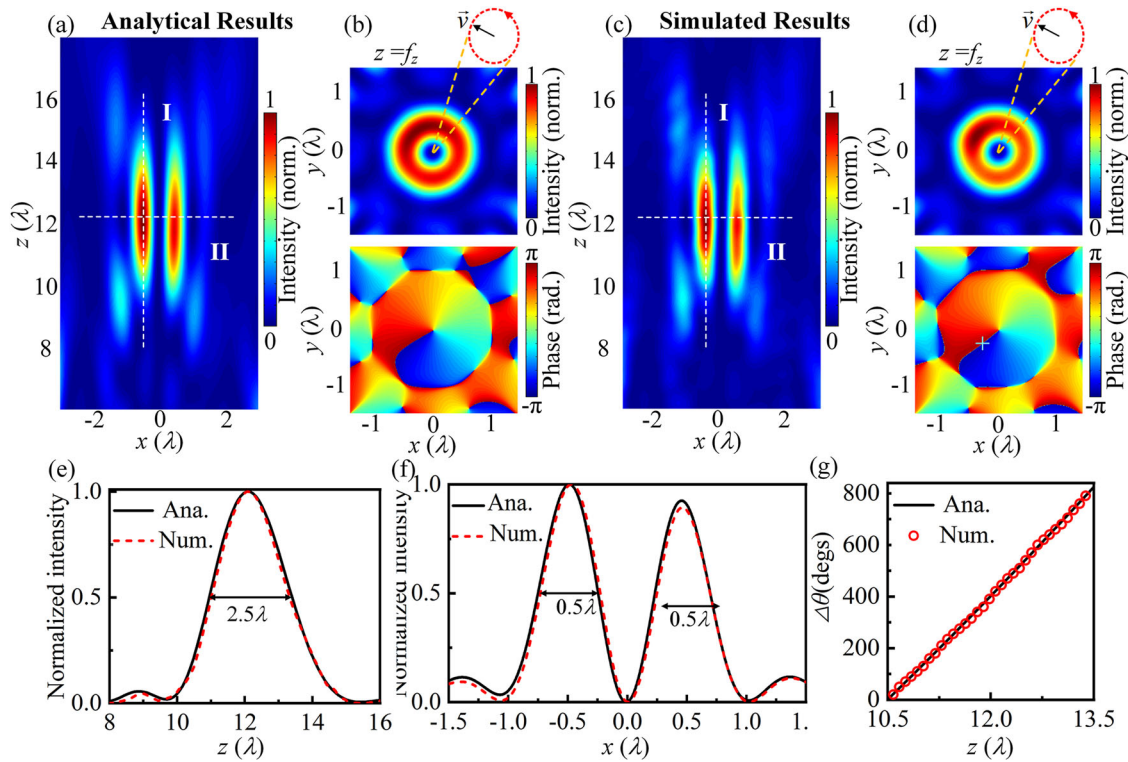
Fig. 3 | Feature analysis of a non-paraxial focused acoustic vortex (NFAV) with $l = 1$. Acoustic phase and intensity distributions of an NFAV with topological charge (TC), $l = 1$ (**a**) in the x–z plane, and (**b**) in the focal plane. The local particle velocity rotates counterclockwise, resulting in a spin-down field. Simulated acoustic phase and intensity distributions of an NFAV with $l = 1$ for TC, (**c**) in the x–z plane, and (**d**) in the focal plane. Acoustic intensity distributions through the focus point along the dashed lines (**e**) I and (**f**) II. **g** Phase rotation angle as a function of z. The black solid and red dashed lines, respectively, represent the analytical and simulated results.

Fig. 3e, f, respectively. It is clear that the NFAV has good focusing performance with respect to the incident beam. In addition, we have studied the phase and intensity distributions in the z-planes near focus ($z = \sim 10.5\lambda$ to $\sim 13.5\lambda$). According to Eq. (8), the spatial phase of an NFAV rotates in a manner described

$$\Delta\theta(z) = \int k_z dz = \frac{2\pi}{\lambda}\left(\sqrt{r_0^2 + z^2} - \sqrt{r_0^2 + z_0^2}\right), \quad (11)$$

where z_0 is the starting z-axis position of the calculation area. In the numerical simulation, we first selected the NFAV at z_0 (10.5λ) and used the position with phase 0 on its toroidal maximum intensity distribution as the initial position. Numerical simulations were performed to obtain the location of phase 0 on the maximum intensity ring at different x-y sections in the z range from 10.5λ to 13.5λ, and to find the angle at which it is rotated with respect to the initial position (using the z-axis as the center of the circle). The theoretical predictions (solid black line) and simulated results (red circles) of the phase angular position during propagation are shown in Fig. 3g. The value of the angle of rotation of the phase angle position with increasing propagation distance indicates the decomposition of the wavenumber k. For simplicity, we employed an artificial structural plate engraved with a finite number of circular holes to generate the DSAB. We should note that the increased circular holes radius and additional circular holes positioned at different angles can effectively improve the power efficiency of our design.

Acoustic spin-controlled orbital rotation

The propagation constant (k_z) decomposition implies that different α values accumulate phase at different rates with propagation distance. We further superimpose two NFAVs with the same focal length, opposite TCs ($l_a = -l_b$), and different cone angles (α_a and α_b) to realize acoustic SOR. The coupling

of two NFAVs near the focusing region can be expressed as

$$P_{SOR}(\rho, \theta, z, t) = P_a + P_b = \exp(-i\omega t)\Big[A_a \exp(ik_{za}z)\exp(il_a\theta)J_{l_a}(k_{ra}\rho)$$
$$+ A_b \exp(ik_{zb}z)\exp(-il_a\theta)J_{-l_a}(k_{rb}\rho)\Big], \quad (12)$$

where $k_{za} = k\cos(\alpha_a)$ and $k_{zb} = k\cos(\alpha_b)$. Two NFAVs are both produced by 56 circle holes and have the same focal length of 280 mm. Since the two NFAVs have different cone angles and opposite TCs, the magnitude of the transverse velocity field on the propagation axis of the two NFAV beams is different and the spin handedness is opposite. When two beams are superimposed, a transverse elliptically polarized velocity field is generated, and the spin handedness after superposition is determined by the spin handedness of the beam with the larger cone angle. By approximating $A_a^2 \approx A_b^2$ and $J_{l_a}(k_{ra}\rho) \approx J_{l_a}(k_{rb}\rho)$, the intensity of the coupled NFAVs can be written as[38]

$$I(\rho, \theta, z) = |P(\rho, \theta, z)|^2 \propto 4A_a^2 J_{l_a}^2(k_{ra}\rho)\cos^2\Big[|l_a|(\theta + \sigma_0|\eta|z)\Big], \quad (13)$$

where $\eta = (k_{za} - k_{zb})/2l_a$ and σ_0 is the polarization mode (left-handed or right-handed polarization) of the NFAV beam with a larger cone angle. According to Eq. (13), the spatial intensity profile rotates with z-axis. Spatial intensity distribution consists mainly of the superposition of the ring-shaped intensities of two NFAVs with helical phases. From Eq. (10), it can be seen that the SAM vanishes in the ring-shaped intensity of the NFAV and there is only the OAM. The number of high-intensity lobes is controlled by TC (which is directly related to OAM) and is equal to $N = |2l_a|$. The direction of rotation can be determined by the polarization elliptic pattern (left- or right-handed polarization) of the superimposed velocity field. That is, the spatial profile rotates with z, in the direction controlled by the spin, by an angle of $\sigma_0 \int |\eta| dz$. Therefore, the form of the rotation is spin-controlled
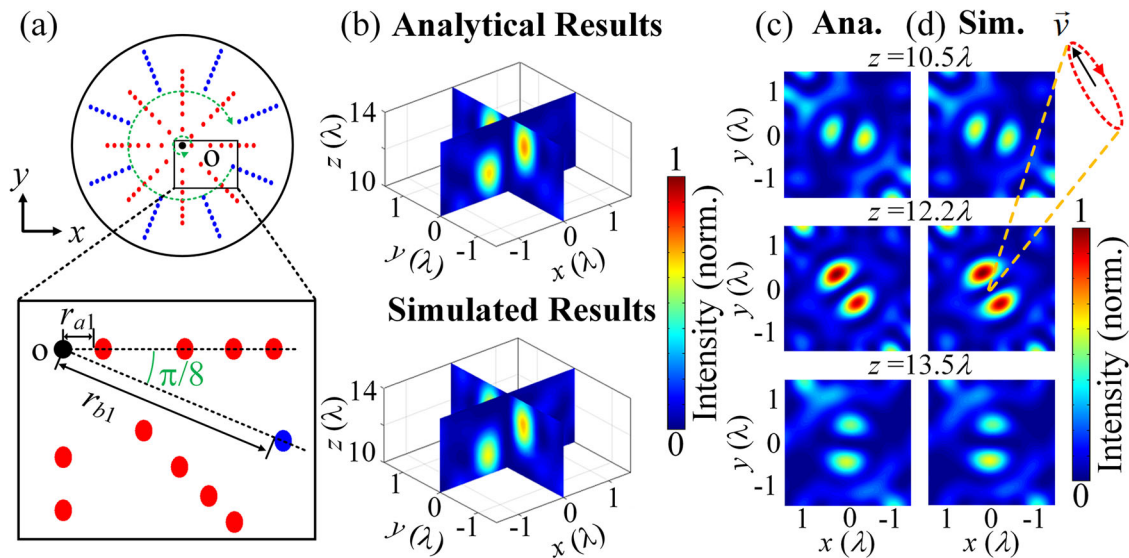
Fig. 4 | The realization of the double spiral acoustic beam (DSAB). a Schematic diagram of the artificial structure engraved with 112 holes. Red circular holes and blue circular holes can generate non-paraxial focused acoustic vortices (NFAVs) with topological charge (TC) of $l_a = 1$ and $l_b = -1$, respectively. r_{a1} and r_{b1} denote the distance from the first red and blue holes to point O, respectively. **b** Analytical and simulated spatial distributions of the intensity field of the artificial structure. **c** Analytical and **d** simulated acoustic intensity maps at three transverse planes of $z = 10.5\lambda$, $z = 12.2\lambda$, and $z = 13.5\lambda$.
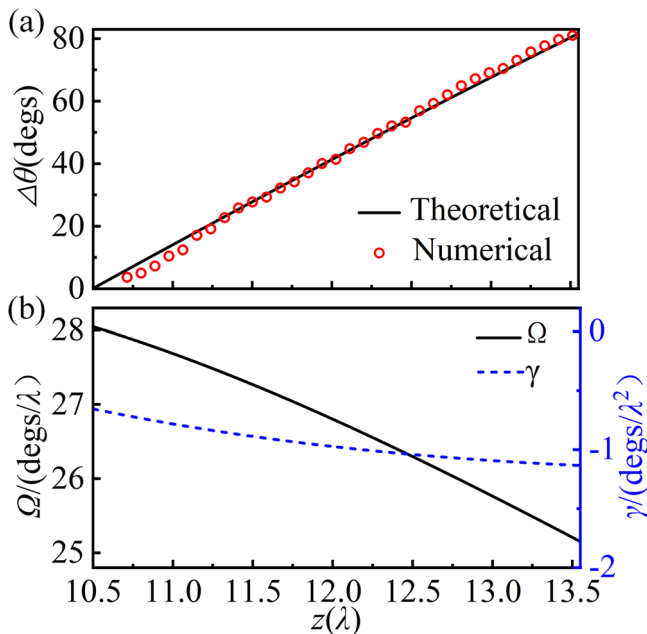
Fig. 5 | The rotation mode of the double spiral acoustic beam (DSAB). a High-intensity lobes rotation angle as a function of z. The black solid line and the red circle indicate the theoretical and numerical results, respectively. **b** The black solid line on the left scale and the blue dashed line on the right scale represent the angular velocity Ω and angular acceleration γ with the propagation distance z, respectively.

orbital rotation and the spatial intensity distribution can be represented in space as a DSAB.

To realize the DSAB, we superimpose two AFS plates respectively engraved with 56 circle holes, as shown in Fig. 4a. One set of 56 circle hole (red) generates a NFAV with TC of $l_a = 1$ and the focal length of $f_z = 280mm$ (12.2λ), where the distance from the first circular hole to point O is $r_{a1} = 40mm$ and thus the cone angle is $\alpha = \sim 39.5°$. Another set of 56 circle holes (blue) produces a NFAV with TC of $l_b = -1$ and the focal length of $f_z = 280mm$ (12.2λ), where the distance from the first circular hole to point O is $r_{b1} = 240mm$ and thus the cone angle is $\alpha = \sim 51.4°$. The crossing

angle between two sets of circle holes is fixed at $\pi/8$ The upper panel of Fig. 4b shows the normalized analytical acoustic intensity distributions on two orthogonal planes. The background medium is air and the working frequency is 15 kHz. It is clearly seen that the locations of the acoustic intensity maximums vary along the z-axis. Then, we perform the full-wave simulations based on the finite-element method. The radius of the circle hole a is fixed at 5 mm and the material of the AFS is set as acoustically rigid. The lower panel of Fig. 4b shows the normalized simulated acoustic intensity distribution, which is in accord with the analytical results. Figure 4c, d show the analytical and simulated acoustic intensity profiles at three transverse planes of $z = 10.5\lambda$, $z = 12.2\lambda$, and $z = 13.5\lambda$, respectively. There are two high-intensity points that gradually rotates with the propagation distance. The simulated velocity field profile has a clockwise elliptical polarization at the center of the NFAV, as shown in the enlarged drawing of Fig. 4d, which is consistent with the theoretical prediction.

According to Eq. (13), the high-intensity lobes rotate in a manner that can be calculated by

$$
\begin{aligned}
\Delta\theta(z) &= \int |\eta| dz = \int \left| \frac{\Delta(k_{za}, k_{zb})}{2l_a} \right| dz \\
&= \frac{\pi}{\lambda} \left| \left(\sqrt{r_{a0}^2 + z^2} - \sqrt{r_{a0}^2 + z_0^2} \right) - \left(\sqrt{r_{b0}^2 + z^2} - \sqrt{r_{b0}^2 + z_0^2} \right) \right|,
\end{aligned}
\tag{14}
$$

where z_0 is the starting z-axis position of the calculation area. In Fig. 5a, the solid line shows the variation of the theoretical angular position of the acoustic intensity maximums with the propagation distance. The nonlinear variation of the angular position means the rotation of the focus is carried out at a variable speed. In the numerical simulations, we first selected the intensity distribution at z_0 (10.5λ), which has two high-intensity lobes. The strongest point in the two high-intensity lobes is symmetric about the center point (on the z-axis), and we use the line connecting the two strongest points as the initial line segment. Numerical simulations were performed to obtain the lines connecting the two strongest points at different $x–y$ sections in the z range from 10.5λ to 13.5λ, and to find the angle at which it is rotated with respect to the initial line segment (using the z-axis as the center of the circle). The circular line represents the simulation results, which matches well with the theoretical results. Figure 5b shows the angular velocity Ω (solid line for left-hand scale) and angular acceleration γ (dashed line for right-hand scale) of this rotation as a function of z. The angular velocity $\Omega = \theta'(z)$ and the angular acceleration $\gamma = \theta''(z)$ can be obtained by computing the first and
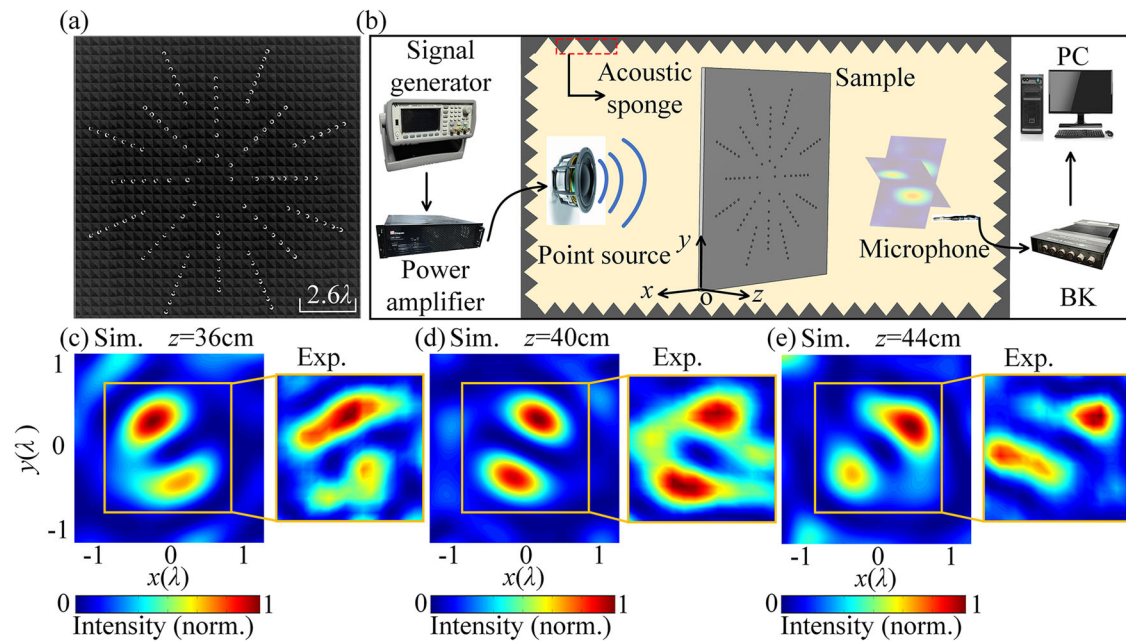
Fig. 6 | The experimental process and result presentation of the double spiral acoustic beam (DSAB). a Photograph of an artificial structure plate sample for realizing DSAB. **b** Experimental setup. The experimental system is mainly composed of seven pieces of equipment: the composite AFS, signal generator, power amplifier, loudspeaker, movable microphone, 3D stepper motor, and multi-analyzer system. Measured and simulated acoustic intensity distributions at three transverse planes of (**c**) z = 36 cm (15.7λ), (**d**) z = 40 cm (17.5λ), and (**e**) z = 44 cm (19.2λ).

second derivatives in Eq. (14) with respect to z, respectively. It is found that, with increasing z-value from 10.5λ to 13.5λ, the Ω decreases from ~28 degs λ^{-1} to ~25 degs λ^{-1} and the corresponding γ increases from ~-0.7 degs λ^{-2} to ~-1.1 degs λ^{-2}. During the high-intensity lobes rotation, the power is exchanged between the main lobes and the side lobes to conserve the angular momentum[39,40]. The main lobes with higher intensities are located at the center of the beam and the side lobes with lower intensities are spread over a larger area. Due to the exchange of power, the main and side lobes take turns to accelerate or decelerate and thus the angular momentum of the entire acoustic field remains constant.

Experimental demonstration

Finally, we fabricate the composite ASF to verify the DSAB and the corresponding acoustic SOR. Figure 6a exhibits the photograph of the composite AFS discussed in Fig. 4, which is fabricated with polymethyl methacrylate. There are 112 round holes engraved on this plate and the geometric size of this sample is $100 \times 100 \times 0.8$ cm³. The experimental setup is depicted in Fig. 6b. For a detailed discussion of this section, please see the Methods below. Figure 6c–e shows the normalized simulated and measured acoustic intensity distributions with N = 2 at three transverse planes of z = 36 cm (15.7λ), z = 40 cm (17.5λ), and z = 44 cm (19.2λ), respectively. In three transverse planes, two identical high-intensity acoustic spots (main lobes) are visible, and they rotate with the propagation distance to produce a DSAB. Both the direction and rotation angle are consistent with the theoretical predictions. These observations suggest that this orbital rotational wave comes from spin coupling. In the experiments, the incident acoustic wave generated by a single loudspeaker is a quasi-plane wave, which is the main reason for the deviation between the simulations and the experiments. In addition, the imprecision of the 3D stepper motor, sample fabrication error, and inevitable viscous effect may have an impact on the measured results.

Conclusion

NFAV beams are considered to be the eigenmodes of total angular momentum operators[21]. The interconversion between SAM and OAM of the NFAV is accompanied by a decomposition of the propagation constant (axial wave vector), distinguished by the value of cone angle. On this basis,

we first designed an artificial structure engraved with discrete circular holes to convert acoustic plane waves into NFAV beams. It is found that the focal length, TC and propagation constant (k_z) of the NFAV can be adjusted by changing the coordinate position of the circular holes. We then superimpose two NFAVs with the same focal length, opposite TCs, and different cone angles to unbind the TCs and acoustic spins, thereby generating a DSAB that enables acoustic SOR to occur. The DSAB and acoustic SOR realized by artificial structural plates are verified by theoretical analysis, numerical simulations, and experimental results. Our scheme offers a simple and effective approach for realizing acoustic SOR, which provides new perspectives and functions for sound manipulation. The achieved intensity rotational profile has potential application value in the operation of small particles, ultrasound therapy and imaging.

Methods

The numerical simulations are performed by using finite element method (FEM) based on COMSOL Multiphysics 5.6 software. The working frequency is fixed at 15 kHz and the background medium is air, the mass density and sound speed of it is ρ_a = 1.21 kg/m³ and c_a = 343.2 m/s. The composite AFS is set to an acoustic hard boundary. Perfectly matched layers (PMLs) are employed to eliminate reflected waves by the outer boundaries. In all simulations, to ensure numerical accuracy, the largest mesh element size is less than one-tenth of the incident wavelength, and further refined meshes are applied in the domain of the composite AFS.

To verify the proposed mechanism, we built an experimental system in an anechoic environment. The system was mainly composed of seven pieces of equipment: the composite AFS, signal generator, power amplifier, loudspeaker, movable microphone, 3D stepper motor, and multi-analyzer system. The composite AFS was made of polymethyl methacrylate with the mass density of 1220 kg m⁻³ and sound speed of 3000 m s⁻¹ which could be thought of as an acoustic hard boundary in air. A loudspeaker (Enpar Type-PD2101) with a central frequency of 15 kHz (λ = ~22.9 mm) was placed at z = 1.4 m to generate an incident quasi-plane wave. A movable microphone (1/4 in., B&K Type-4938-A-011) was attached to a 3D stepper motor with a set of 2.28 mm (0.1λ), and the acoustic field in the target area behind the composite ASF was scanned point by point by this microphone. Meanwhile,

another microphone was set in the transmitted acoustic field as a reference. The measured acoustic signals were then analyzed with a multi-analyzer system (B&K Type-3160-A-042) and then the measured acoustic field was reconstructed. In experiments, the sound velocity and density in the air were set to $c = 340$ m s^{-1} and $\rho = 1.29$ kg m^{-3}, respectively.

Data availability

The data that support the findings of this study are available from the corresponding author upon reasonable request.

References

1. Zhao, Y., Edgar, J., Jeffries, G., McGloin, D. & Chiu, D. Spin-to-orbital angular momentum conversion in a strongly focused optical beam. *Phys. Rev. Lett.* **99**, 073901 (2007).
2. Bliokh, K., Alonso, M., Ostrovskaya, E. & Aiello, A. Angular momenta and spin-orbit interaction of nonparaxial light in free space. *Phys. Rev. A* **82**, 063825 (2010).
3. Shao, Z., Zhu, J., Chen, Y., Zhang, Y. & Yu, S. Spin-orbit interaction of light induced by transverse spin angular momentum engineering. *Nat. Commun.* **9**, 926 (2018).
4. Rodriguez-Herrera, O., Lara, D., Bliokh, K., Ostrovskaya, E. & Dainty, C. Optical nanoprobing via spin-orbit interaction of light. *Phys. Rev. Lett.* **104**, 253601 (2010).
5. Yu, N. & Capasso, F. Flat optics with designer metasurfaces. *Nat. Mater* **13**, 139–150 (2014).
6. Fickler, R. et al. Quantum entanglement of high angular momenta. *Science* **338**, 640–643 (2012).
7. Stav, T. et al. Quantum entanglement of the spin and orbital angular momentum of photons using metamaterials. *Science* **361**, 1101–1103 (2018).
8. Roy, B., Ghosh, N., Banerjee, A., Gupta, S. & Roy, S. Manifestations of geometric phase and enhanced spin Hall shifts in an optical trap. *New J. Phys* **16**, 083037 (2014).
9. Molina, T., Torres, J. & Torner, L. Twisted photons. *Nat. Phys* **3**, 305–310 (2007).
10. Franke, A., Allen, L. & Padgett, M. Advances in optical angular momentum. *Laser Photon. Rev.* **2**, 299–313 (2008).
11. Lloyd, S., Babiker, M., Thirunavukkarasu, G. & Yuan, J. Electron vortices: Beams with orbital angular momentum. *Rev. Mod. Phys.* **89**, 035004 (2007).
12. Bliokh, K. & Nori, F. Transverse and longitudinal angular momenta of light. *Phys. Rep.* **592**, 1–38 (2015).
13. Lai, M., Wang, Y., Liang, G. & Zong, H. Geometrical phase and Hall effect associated with the transverse spin of light. *Phys. Rev. A* **100**, 033825 (2019).
14. Bliokh, K., Rodríguez, F., Nori, F. & Zayats, A. Spin-orbit interactions of light. *Nat. Photon.* **9**, 796–808 (2015).
15. Jiménez, N., Romero, G., García, R., Camarena, F. & Staliunas, K. Sharp acoustic vortex focusing by Fresnel-spiral zone plates. *Appl. Phys. Lett* **112**, 204101 (2018).
16. Fu, Y. et al. Asymmetric generation of acoustic vortex using dual-layer metasurfaces. *Phys. Rev. Lett.* **128**, 104501 (2022).
17. Chen, D., Zhou, Q., Zhu, X., Xu, Z. & Wu, D. Focused acoustic vortex by an artificial structure with two sets of discrete Archimedean spiral slits. *Appl. Phys. Lett.* **115**, 083501 (2019).
18. Yang, Y., Thirunavukkarasu, G., Babiker, M. & Yuan, J. Orbital-angular-momentum mode selection by rotationally symmetric superposition of chiral states with application to electron vortex beams. *Phys. Rev. Lett.* **119**, 094802 (2017).
19. Hefner, B. & Marston, P. An acoustical helicoidal wave transducer with applications for the alignment of ultrasonic and underwater systems. *J. Acoust. Soc. Am.* **106**, 3313–3316 (1999).
20. Thomas, J. & Marchiano, R. Pseudo angular momentum and topological charge conservation for nonlinear acoustical vortices. *Phys. Rev. Lett.* **91**, 244302 (2003).
21. Long, Y. et al. Realization of acoustic spin transport in metasurface waveguides. *Nat. Commun* **11**, 4716 (2020).
22. Shi, C. et al. Observation of acoustic spin. *Natl. Sci. Rev* **6**, 707–712 (2019).
23. Bliokh, K. & Nori, F. Transverse spin and surface waves in acoustic metamaterials. *Phys. Rev. B* **99**, 020301 (2019).
24. Bliokh, K. & Nori, F. Spin and orbital angular momenta of acoustic beams. *Phys. Rev. B* **99**, 174310 (2019).
25. Liu, T. et al. Chirality-switchable acoustic vortex emission via non-Hermitian selective excitation at an exceptional point. *Sci. Bull.* **67**, 1131–1136 (2022).
26. Wang, S. et al. Spin-orbit interactions of transverse sound. *Nat. Commun.* **12**, 6125 (2021).
27. Muelas-Hurtado, R. et al. Observation of polarization singularities and topological textures in sound waves. *Phys. Rev. Lett.* **129**, 204301 (2022).
28. Monteiro, P., Neto, P. & Nussenzveig, H. Angular momentum of focused beams: Beyond the paraxial approximation. *Phys. Rev. A* **79**, 033830 (2009).
29. Bliokh, K., Dennis, M. & Nori, F. Relativistic electron vortex beams: angular momentum and spin-orbit interaction. *Phys. Rev. Lett.* **107**, 174802 (2011).
30. Alhaïtz, L., Brunet, T., Aristégui, C., Poncelet, O. & Baresch, D. Confined phase singularities reveal the spin-to-orbital angular momentum conversion of sound waves. *Phys. Rev. Lett.* **131**, 114001 (2023).
31. Vitullo, D. et al. Observation of interaction of spin and intrinsic orbital angular momentum of light. *Phys. Rev. Lett.* **118**, 083601 (2017).
32. Leary, C., Raymer, M. & van Enk, S. Spin and orbital rotation of electrons and photons via spin-orbit interaction. *Phys. Rev. A* **80**, 061804 (2009).
33. Durnin, J. Exact solutions for nondiffracting beams. I. The scalar theory. *J. Opt. Soc. Am. A* **4**, 651–654 (1987).
34. Marston, P. Scattering of a Bessel beam by a sphere. *J. Acoust. Soc. Am.* **121**, 753–758 (2007).
35. Volke, S., Santillán, A. & Boullosa, R. Transfer of angular momentum to matter from acoustical vortices in free space. *Phys. Rev. Lett.* **100**, 024302 (2008).
36. Jiang, X. et al. Broadband and stable acoustic vortex emitter with multi-arm coiling slits. *Appl. Phys. Lett.* **108**, 203501 (2016).
37. Wang, T. et al. Particle manipulation with acoustic vortex beam induced by a brass plate with spiral shape structure. *Appl. Phys. Lett.* **109**, 123506 (2016).
38. Vetter, C., Eichelkraut, T., Ornigotti, M. & Szameit, A. Optimization and control of two-component radially self-accelerating beams. *Appl. Phys. Lett.* **107**, 211104 (2015).
39. Schulze, C. et al. Accelerated rotation with orbital angular momentum modes. *Phys. Rev. A* **91**, 043821 (2015).
40. Webster, J., Rosales, G. & Forbes, A. Radially dependent angular acceleration of twisted light. *Opt. Lett.* **42**, 675–678 (2017).

Author contributions

D.C. Chen, X. Liu, D.J. Wu studied the methods. D.C. Chen, X. Liu, D.J. Wu did the investigation. D.C. Chen, D.J. Wu, X.J. Liu supervised and wrote the article. X. Liu carried out the experiments. X.F. Zhu, Q. Wei, Y. Cheng co-discussed the program. All authors contributed to the data analysis and discussion.

Competing interests

The authors declare no competing interests.

Additional information